Monitoring of Urban Impervious Surfaces Using Time Series of High-Resolution Remote Sensing Images in Rapidly Urbanized Areas: A Case Study of Shenzhen

Tao Zhang and Xin Huang, *Senior Member, IEEE*

***Abstract*—Knowledge of impervious surface changes is important for understanding the urban environment and human activity. Most of previous studies have investigated impervious surface change at a macro level (e.g., urban expansion) using medium-resolution images but ignored the subtle changes within urban areas. High-resolution images have great potential to precisely monitor the detailed characteristics of impervious surfaces. However, very few studies focused on this issue using multitemporal high-resolution data. In this study, we aimed to resolve these problems and investigate the impervious surface characteristics using high-resolution time-series data. The experiments were performed on Shenzhen, a megacity in China that has experienced rapid urbanization over the past three decades. The images were acquired by QuickBird (2.4 m), WorldView-2 (2 m), and WorldView-3 (1.2 m) at ∼2-year intervals from 2003 to 2017. The presented method integrating multiple features was found to be effective in extracting impervious surfaces from the high-resolution images (kappa coefficient greater than 0.90), and the average accuracy of the change detection was 75%. Courtesy of the high-resolution imagery, it was revealed that the impervious surfaces can be converted back to pervious surfaces, and some regions have shown repeated changes due to the urban renewal planning. It was also found that impervious surfaces in Shenzhen gradually increased before 2012, but subsequently showed a decreasing tendency, reflecting the adjusted strategies for urban development. Our results demonstrate that high-resolution images are essential for precise impervious surface monitoring, and can provide deep insights into urban development patterns during the process of urbanization.**

***Index Terms*—Change detection, high-resolution images, impervious surfaces, time-series analysis, urban.**

Manuscript received September 29, 2017; revised January 3, 2018; accepted February 5, 2018. This work was supported by the National Key R&D Program of China under Grant 2017YFB0504103, the National Natural Science Foundation of China under Grant 41522110 and Grant 41771360, and the Hubei Provincial Natural Science Foundation of China under Grant 2017CFA029. *(Corresponding author: Xin Huang.)*

T. Zhang is with the State Key Laboratory of Information Engineering in Surveying, Mapping, and Remote Sensing, Wuhan University, Wuhan 430079, China (e-mail: zhangtao437@163.com).

X. Huang is with the State Key Laboratory of Information Engineering in Surveying, Mapping, and Remote Sensing, Wuhan University, Wuhan 430079, China, and also with the School of Remote Sensing and Information Engineering, Wuhan University, Wuhan 430079, China (e-mail: huang_whu@163.com; xhuang@whu.edu.cn).

Color versions of one or more of the figures in this paper are available online at http://ieeexplore.ieee.org.

Digital Object Identifier 10.1109/JSTARS.2018.2804440

I. Introduction

IMPERVIOUS surfaces are generally defined as artificial materials that water cannot infiltrate, and are mainly associated with buildings and transportation (e.g., street, pavement, parking lot) [1]. Although currently occupying only a small proportion of Earth's terrestrial surface, impervious surfaces have a great impact on human beings. Besides being a primary component of urban land cover and an important indicator of the degree of urbanization, impervious surfaces also significantly affect the urban environment, such as surface runoff, air quality, and the urban heat island effect [2], [3]. In recent years, the developing countries (e.g., China) have undergone rapid urbanization, with frequent changes related to impervious surfaces. Apart from urban expansion, the subtle changes of impervious surfaces within urban areas are also very common due to the construction and demolition of buildings in the process of urban development [4]. Knowledge of such detailed characteristics of impervious surfaces across time-series data is highly desired since it can help us to understand the urbanization process and make proper urban planning proposals. Accordingly, the accurate and detailed monitoring of impervious surfaces is of great importance for many urban- and environment-related applications.

The remote sensing technique has been widely applied in the monitoring of urban impervious surfaces, due to its large-scale coverage and high temporal frequency [5]. Motivated by the significance of impervious surfaces, numerous studies have focused on impervious surface monitoring using remote sensing data, most of which have employed medium-resolution satellite images such as the Landsat series [3], [6]. Because of the mixed pixel effect caused by the limited spatial resolution and the complicated urban landscapes, the results extracted from medium-resolution images usually have limited accuracy [2]. More importantly, these studies have mainly focused on impervious surface change at a macro level (e.g., urban expansion), based on the assumption that impervious surfaces are rarely converted back to pervious surfaces [5], [7]. However, in fact, this assumption is not always satisfied during the process of rapid urbanization in developing countries. For instance, Shenzhen in China, which was a small fishing village in the 1970s, has now developed into a large modern city, resulting in a large number of complicated urban land-cover and land-use changes.

Moreover, in recent years, the Chinese government has paid increasing attention to protecting the urban environment and promoting ecosystem services [8]. It is now common that impervious surfaces are converted back to pervious surfaces with a stronger ecological function during the process of urban development. In addition, some regions may have changed more than once due to the urban renewal policies (e.g., demolition of old buildings and reconstruction of new architecture) [9]. Accordingly, the assumption of irreversible urban transition is not suitable when dealing with frequent urban changes, and the traditional medium-resolution data fail to effectively capture such impervious surface change information within urban areas [4].

In recent years, the availability of multitemporal high-resolution imagery provided by different satellite sensors such as QuickBird and WorldView has offered a new opportunity for detailed impervious surface trajectory monitoring within urban areas, e.g., demolition and reconstruction of urban infrastructure at different times but the same location, and hence supports a more in-depth understanding of urban development patterns [10]. Some related studies have investigated urban land-cover changes through bi-temporal comparison [11], [12], but very few studies have focused on the monitoring of impervious surfaces using time series of high-resolution images to characterize the change profiles of impervious surfaces within urban areas. This can be attributed to the data availability and the large spatial heterogeneity in multitemporal high-resolution images (e.g., different viewing angles, illumination conditions, spatial registration errors, and different shadow sizes and shapes). These issues make it difficult to detect accurate and reliable changes from high-resolution imagery. It is widely acknowledged that change detection at the pixel level can lead to a large number of false alarms when conducting change analysis from high-resolution images of complicated urban landscapes [13], [14]. Therefore, in this study, we performed impervious surface monitoring based on the grid level, which can mitigate the spatial heterogeneity in the multitemporal high-resolution images. This strategy is also called hot-spot detection, which has been used in some studies when dealing with change detection from high-resolution images [11], [15], [16].

In the meantime, the accurate multitemporal extraction of impervious surfaces is also of great importance since it provides an underlying basis for the subsequent time-series analysis. Although the high-resolution images provide great potential to extract much more detailed impervious surface information, new problems (e.g., the high spectral variation of impervious surfaces and the shadows caused by high buildings) arise with these image data [1]. Different methods, including pixel-based and object-based methods, have been developed to extract impervious surfaces from high-resolution images [2], [17]. Many studies have demonstrated that the object-based methods outperform the pixel-based methods [18], [19]. Specifically, in some studies, the shaded areas are treated as a single class or further classified to reduce the impact of shadows [20], [21]. However, the accurate extraction of impervious surfaces from high-resolution images remains a big challenge, and in the current research, the abundant spatial information (e.g., textural, shape information) inherent in high-resolution data and the semantic information of the shaded areas (e.g., class-related spatial relations) have not been fully investigated to promote the accuracy of impervious surface mapping. For instance, the spatial and semantic features can complement each other by characterizing image properties from different perspectives to improve the discrimination among spectrally similar objects (e.g., bright impervious surfaces and soil; dark impervious surfaces and water and shadow). Accordingly, in this study, we attempted to use multiple features, including spectral, textural, shape, and class-related features, for impervious surface extraction. The proposed multifeature framework can make full use of the information provided by the high-resolution images to produce a more accurate estimation of impervious surfaces.

In summary, this study was aimed at addressing the key issues for the monitoring of impervious surfaces within urban areas using time series of high-resolution data. The method was applied in multitemporal images of Shenzhen, a typical megacity in China, at ∼2-year intervals from 2003 to 2017. The research objectives of this study were:

1) accurate impervious surface extraction using the multiple features inherent in high-resolution data to deal with the land-cover confusion and shadow problems;
2) investigation of the detailed characteristics of impervious surfaces spanning 15 years (e.g., location, type, and frequency of change) in Shenzhen;
3) analysis of the urban development pattern in Shenzhen during the past years (e.g., infrastructure construction, ecosystem services promotion, and urban renewal).

II. Study Area and Data Sets

In this study, Shenzhen, a typical megacity in China, was selected for the monitoring of urban impervious surfaces. Shenzhen, located in Guangdong province, is one of the largest cities in the Pearl River Delta. As China's first special economic zone, it has experienced astonishing economic and urban development, from a tiny rural town to a large city with a population of more than 10 million over the past 30 years [22]. A number of complicated impervious surface changes have taken place during the process of rapid urbanization. Therefore, the urban area of Shenzhen was appropriate for our research into impervious surface change investigation.

We collected a series of high-resolution remote sensing images of Shenzhen at ∼2-year intervals from 2003 to 2017 (see Fig. 1 and Table I). The images covered ∼100 km^2, including the main urban areas of Shenzhen, with various landscapes, e.g., hill, river, park, high-rise commercial architecture, and low-rise residential buildings such as urban villages [23]. The satellite sensors included QuickBird (2.4 m), WorldView-2 (2 m), and WorldView-3 (1.2 m). In Fig. 1(c), it can be clearly seen that a large building was demolished in 2012, but some new architecture was rebuilt in 2015 at the same location, which indicates that repeated land-cover changes can occur during the process of urban development. Fortunately, the time series of high-resolution images of Shenzhen spanning 15 years provided us with great potential to monitor the detailed characteristics of impervious surfaces within the urban areas. In the preprocessing step, the raw digital number (DN) values of the remote sensing images

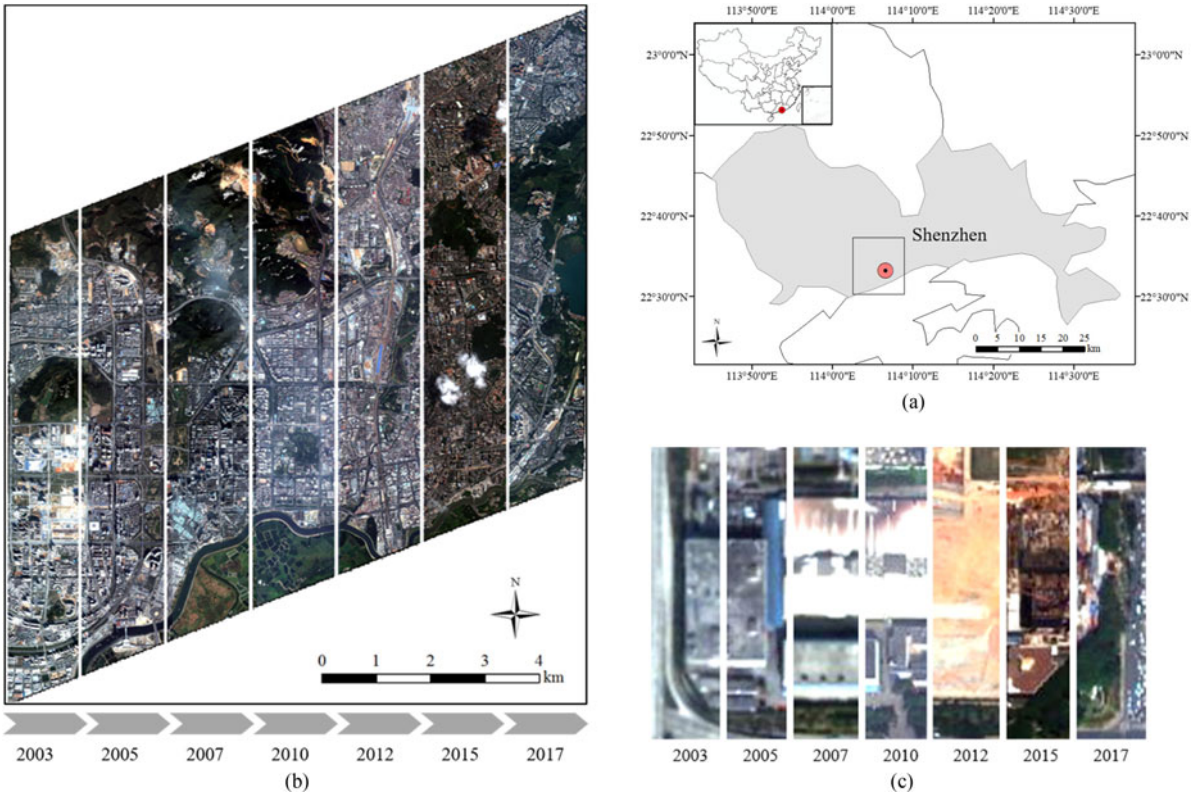

Fig. 1. Study area and data sets. (a) Overview of the study area for Shenzhen city. (b) The high-resolution time-series images used in this study. Note that all the images can cover the whole study area. (c) Local scene composed of seven pieces. Each piece (taken at different times) shows a part of the whole scene.

TABLE I
SUMMARY OF THE DETAILED INFORMATION FOR THE DATA SETS CONSIDERED IN THIS RESEARCH

Image	Date	Sensor	Spectral range
Shenzhen 2003	2003/01/07	QuickBird	4 bands 450–900 nm
Shenzhen 2005	2005/12/17		
Shenzhen 2007	2007/12/10		
Shenzhen 2010	2010/11/03	WorldView-2	8 bands 400–1040 nm
Shenzhen 2012	2012/03/25		
Shenzhen 2015	2015/08/04	WorldView-3	8 bands 400–1040 nm
Shenzhen 2017	2017/02/18	WorldView-3	16 bands 400–2365 nm

were converted to surface reflectance with the FLAASH atmospheric correction module embedded in ENVI software, to reduce the effect of the atmosphere [24]. The low-quality observations (e.g., cloud and haze) were manually masked out and all the images were resampled to 2-m resolution for the subsequent processing and analysis. All the spectral bands available for each image were used when conducting the classification. In addition, since evergreen broadleaf species are prominent in Shenzhen, the seasonal variation has no significant effect on impervious surface change.

III. METHODS

In this study, we investigated the detailed characteristics of impervious surfaces using multiple high-resolution images. First, a series of accurate impervious surface maps were generated using the multifeature object-based approach to provide an underlying basis for the impervious surface monitoring. A grid-level approach, which can mitigate the spatial heterogeneity in high-resolution images, was then employed to detect the impervious surface changes across the time series. Finally, the continuous change profiles of the impervious surfaces were further investigated and analyzed.

A. Object-Based Impervious Surface Mapping Using Multiple Features

1) Class Definition: Mapping impervious surfaces can be regarded as a classification task, where impervious/pervious surfaces consist of various land-cover materials. For instance, impervious surfaces can be made up of bright materials (e.g., metal and new concrete) and dark materials (e.g., asphalt and old concrete), while pervious surfaces mainly refer to vegetation, water, and bare soil [25]. In this study, a two-stage object-based classification approach was proposed for extracting the impervious surfaces (see Fig. 2). First, six land-cover types, i.e., bright impervious surface, dark impervious surface, shadow, soil, vegetation, and water, were identified. Note that the shadows were regarded as a single land-cover type since they often present unique spectral and spatial properties [26]. Moreover, the shaded areas may consist of both impervious (e.g., roads and roofs) and pervious surfaces (e.g., vegetation), which can have a great impact on accurate impervious surface extraction. Therefore, in the second stage, the shadows were further classified into shaded impervious surfaces and shaded pervious surfaces.

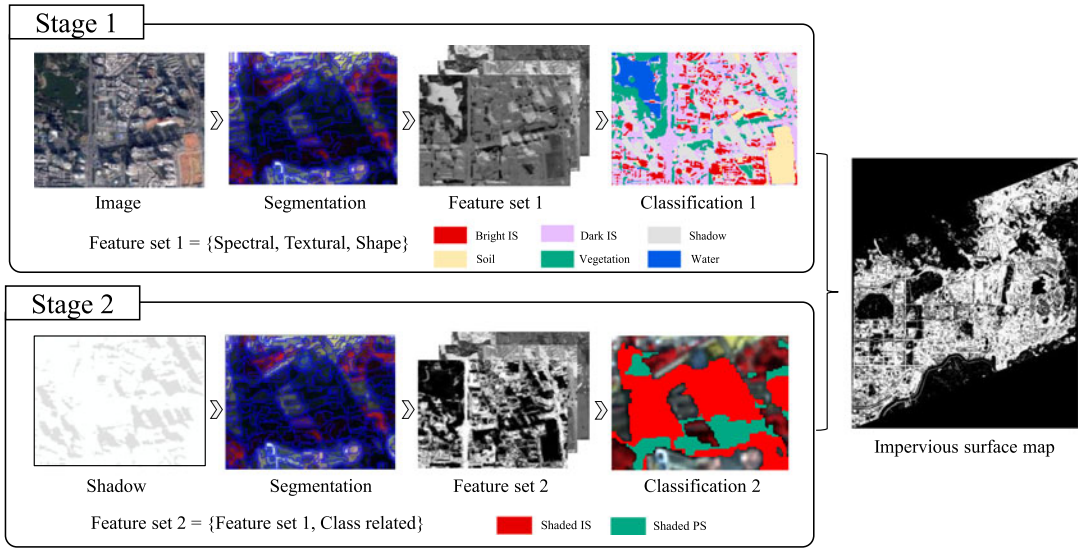

Fig. 2. Multifeature classification framework for impervious surface mapping (IS = impervious surface, PS = pervious surface).

Finally, bright impervious surface, dark impervious surface, and shaded impervious surface were combined as "impervious surfaces", while the other land covers were viewed as "pervious surfaces".

2) Feature Extraction and Object-Based Classification: Image segmentation is a prerequisite step to object-based classification. In this study, the time-series images were segmented into relatively homogeneous objects using a multiresolution segmentation algorithm [27]. In the first stage, the segmentation was conducted at a relatively small scale parameter (e.g., 50), determined by visual interpretation of the image segmentation results and some other related research [26]. At this scale, the objects were viewed as relatively homogenous regions, i.e., all the pixels within an image object belonged to one land-cover class. The multiple features, including spectral, textural, and shape features, were then extracted. The spectral features can record the spectral reflectance of the different land-cover materials, and include mean spectral reflectance, vegetation index, etc. The textural features have the ability to describe the tonal variations of different land covers to assist the classification, e.g., water and shadow have very similar radiometric responses, but water usually has a smaller variance than that of shaded areas [26]. The textural features include the gray-level co-occurrence matrix (GLCM) measures (e.g., homogeneity, and contrast) [28], and morphological metrics such as the morphological building index/shadow index, which can characterize the building or shadow components in high-resolution images [29]. The GLCM measures were calculated based on the panchromatic image for the individual image objects. The spatial displacement was set as a distance of one in four directions (0°, 45°, 90°, 135°), and subsequently, the directionality was suppressed by averaging the extracted features over the four directions [30].The shape features, e.g., border length, and shape index, can be used to measure the geometric characteristics of image objects such as elongated roads and ponds. In the second stage, only the shadows were focused on, and they were further segmented at a smaller scale parameter (set to 30 in this study), at which the shaded areas could be segmented into smaller objects to alleviate the mixed-object effects for shaded areas [21], [26]. Shadows can obscure impervious surfaces and increase the difficulty of correctly identifying the shaded impervious surfaces. In view of this, the semantic information, i.e., the class-related features, was considered as an additional feature set in the shadow classification. For instance, when a shaded object is much closer to vegetation, it is more likely to be vegetation and, hence, the class-related features can benefit the shadow classification. In addition, for the convenience of the subsequent change analysis, the shaded pervious objects were further classified into the specific class (i.e., soil, vegetation, and water) to which they had the smallest distance. In most cases, it seems impossible to select the one optimal feature set for different objects and scenes. Consequently, image classification integrating multiple features (see Table II) was attempted in this study, to enable more accurate mapping of impervious surfaces.

In this study, the random forest (RF) algorithm was selected as the classifier since it has been widely applied in remote sensing studies and yields accurate land-cover maps [25], [31]. RF is a well-known ensemble learning method for classification, which is operated by constructing multiple decision trees and outputting the class through majority voting from all the individual trees [25]. It has been demonstrated that RF can achieve a classification accuracy that is comparable to the traditional methods such as support vector machine (SVM) [32]. Moreover, RF has a great ability to deal with large data sets and extremely high dimensional input feature spaces [33], and hence was used to perform the classification procedure with multiple features in this study. The classification in this study was conducted in each time series separately.

B. Monitoring of Impervious Surfaces

1) Basic Units for Change Detection: Change detection can be conducted using the multitemporal impervious surface maps spanning the 15 years. However, the large spatial heterogeneities

TABLE II
MULTIPLE FEATURES USED IN THE CLASSIFICATION

Feature type	Feature name	Feature description
Spectral	[Mean band]	The average intensity on each spectral band
	[Std. dev]	The standard deviation on each spectral band
	[Brightness]	The average intensity of all the spectral bands
	[Max. diff.]	The maximum difference of the average intensity of each band to the brightness
	[NDVI/NDWI]	Normalized difference vegetation index/water index
	[HIS]	The hue, intensity, and saturation of RGB color
Textural	[Mean]	Average of gray level
	[Variance]	Gray-level variance
	[Homogeneity]	The homogeneity derived from the GLCM
	[Contrast]	The contrast derived from the GLCM
	[Dissimilarity]	The dissimilarity derived from the GLCM
	[Entropy]	The entropy derived from the GLCM
	[Second moment]	The second moment derived from the GLCM
	[Correlation]	The correlation derived from the GLCM
	[MBI/MSI]	Morphological building index/shadow index
Shape	[Area]	The number of pixels within image objects
	[Border length]	The number of pixels of the inner and outer borders
	[Length/width]	The length-width ratio of the bounding box
	[Asymmetry]	The relative length of an image object compared to a regular polygon
	[Border index]	The ratio of the border lengths of an image object to the smallest enclosing rectangle
	[Compactness]	The ratio of the product of length and width to the area of an image object
	[Density]	The number of pixels of an image object divided by its approximate radius
	[Ellipse fit]	The degree of an image object fitting into an ellipse
	[Radius ellipse]	The radiuses of the largest enclosed ellipse and the smallest enclosing ellipse
	[Rectangular fit]	The degree of an image object fitting into a rectangle
	[Shape index]	The border length of an object divided by four times the square root of its area
	[Roundness]	The difference between the radiuses of the enclosing ellipse and the enclosed ellipse
Class-related	[Rel. Border to]	The relative length of the shared border of an image object to one class
	[Rel. Area of]	The relative area of one class within a circular area
	[Distance to]	The distance of the image object to the closest image object of one class

in the high-resolution time-series images, including different viewing angles, spatial registration errors, and complicated urban landscapes, make it difficult to detect accurate and reliable change information, and can often lead to a large number of false alarms when conducting change analysis from high-resolution images at the pixel level [10], [34]. In this context, we therefore employed a grid-level approach to monitor the impervious surface change, which is aimed at discovering changed scenes rather than individual pixels [23]. This strategy is also called hotspot detection, and has been used in related studies for change detection from high-resolution images [11], [15], [16]. In this study, the image was initially divided into a series of grids, which were regarded as the basic units for change detection. The proportion of impervious surfaces in each grid was calculated, and thus the binary map of impervious surfaces was converted to an impervious surface percentage map for the subsequent processing and analysis. The grid size in this study was set as 200 m for the following reasons. The sizes of the largest buildings (e.g., large residential buildings and public facilities) in the image ranged from 100 m to 150 m. Moreover, due to the various viewing angles in the multitemporal high-resolution imagery, the tall buildings may incline toward different directions, and the cast shadows may have different shapes and sizes [10]. The selected grid was expected to cover the urban scene, including buildings and their surroundings (e.g., roads, shadows, and vegetation). Thus, the size of the grid should be larger than the size of the large and tall buildings, and 200 m was selected as a suitable value in this regard.

2) Change Detection Based on Median Absolute Deviation: In this study, a change detection method based on median absolute deviation (MAD) [35] was used to detect the changes across the time series. In general, the impervious surface area in most multitemporal images is relatively stable, and the significant change can be regarded as an outlier in the whole time series [36]. MAD is a robust measure and is immune to sample size [37], and can be used to effectively detect the outliers. The time-series data set can be expressed as:

$$T = \{T(1), T(2), \ldots, T(i)\} \tag{1}$$

$$DT = \{T(2) - T(1), T(3) - T(2), \ldots, T(i) - T(i-1)\} \tag{2}$$

where $T(i)$ means the impervious surface percentage in the image of the ith year; and DT is the time difference between neighboring years. MAD can be defined as follows:

$$\mathrm{MAD} = b \times \mathrm{median}\left\{|\mathrm{DT}(i) - \mathrm{median}(\mathrm{DT})|\right\} \tag{3}$$

where median$(\cdot)$ is the median of the series. Usually, $b = 1.483$, a constant linked to the assumption of normality of the data [37]. Finally, the anomaly degree L is defined as

$$L = \frac{|\mathrm{DT}(i) - \mathrm{median}(\mathrm{DT})|}{\mathrm{MAD}}. \tag{4}$$

A large L value indicates a high degree of change. Generally, the anomaly criteria can be adjusted by the researcher, e.g., Miller [38] suggested a value of 3, 2.5, or 2 for anomaly detection. A larger value indicates a more strict criteria for outlier

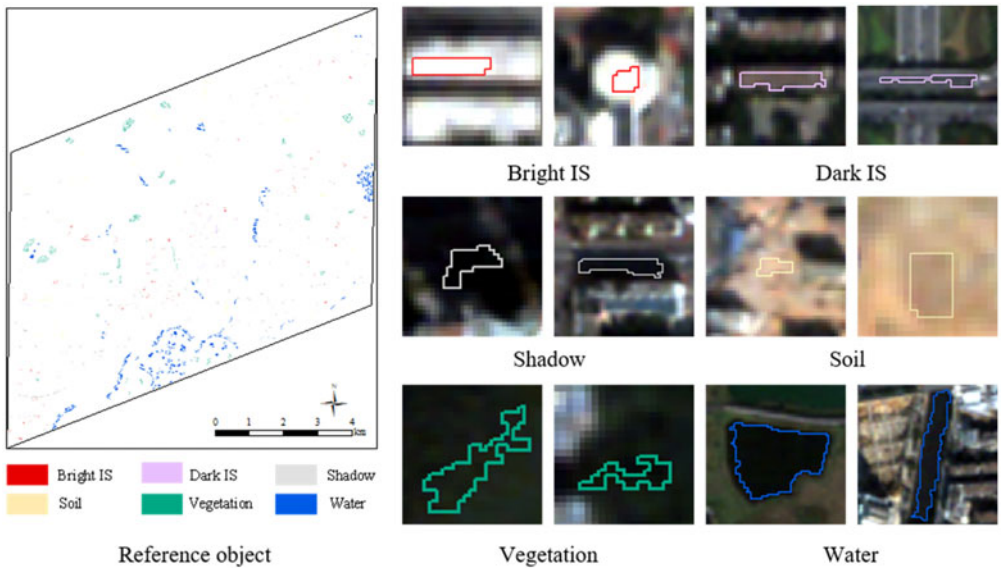

Fig. 3. Reference objects collected for the representative image of Shenzhen 2003 and some representative labeled objects of local areas in general urban land-cover classification (IS = impervious surface). Note that we collected reference samples separately for all the images.

TABLE III
REPRESENTATIVE LANDSCAPE METRICS CONSIDERED IN THIS STUDY

Metric	Description
Largest patch index (LPI)	The percentage of the total landscape that is made up by the largest patch
Mean patch area (MPA)	The average area of the impervious surface within a unit
Patch density (PD)	The number of impervious surface patches per unit area

identification. In this study, we employed a relatively strict strategy for change detection, and hence we chose the threshold of 3 in our experiment [37] to mitigate the false alarms caused by the large spatial heterogeneity (e.g., parallax distortion and viewing angle effect) in the high-resolution images.

C. Grid-Level Landscape Analysis

The urban landscape, which indicates the arrangement, distribution, and spatial characteristic of urban land covers, can be expressed as a series of quantitative indexes. In this research, in order to further measure the spatial distribution of the impervious surfaces across the time series, some representative landscape metrics (see Table III) were calculated, including the largest patch index (LPI), mean patch area (MPA), and patch density (PD), which can quantitatively describe the spatial pattern of impervious surfaces [39]. In this study, the considered landscape metrics were only calculated for impervious surfaces in each image grid. The overall change tendency of landscape metrics can reflect the urban development pattern over the past years.

D. Accuracy Assessment

1) Accuracy Assessment of Impervious Surface Classification: The reference data were manually collected through careful visual interpretation of each high-resolution image. Taking a representative image of Shenzhen 2003 as an example, as shown in Fig. 3, the reference objects, evenly distributed over the whole study area, were collected with a spatial constraint in this study, i.e., each reference object has no common border with the other ones, which means that each labeled object is far away from the others, in order to ensure the spatial independence. For all the collected reference samples, 50% of each class were randomly selected as the training samples to construct the RF model using 300 trees, referring to the current literature [25], [40], and the rest were used as the validation set to test the effectiveness of the classification result (see Table IV). As such, the training samples selected were spatially disjoint from the validation samples. The selection of training samples was undertaken 10 times, and the final classification map for the subsequent change analysis was obtained by majority voting of each classification result. The overall accuracy (OA) and kappa coefficient [41] generated from the confusion matrix were used to assess the accuracy of the impervious surface extraction.

2) Accuracy Assessment of Change Patterns: The accuracy assessment of continuous change patterns is necessary when dealing with multitemporal image analysis. First, the accuracies of the change detection between the neighboring years were evaluated. All the detected changed areas at the grid level were carefully checked on the high-resolution images and, in the meantime, some randomly selected unchanged areas were also included. Due to the relatively large size of the unchanged areas, the number of selected unchanged grids was set to twice that of the changed grids [5] (see Table VII). The confusion matrix for each changed period was then derived for the accuracy evaluation. In addition to the assessment of change detection between the neighboring years, the accuracy across the whole time series was also evaluated. Specifically, the detected changed years were flagged as 1 and the unchanged years were labeled as 0. A long string composed of 0 and 1 was then generated for each detected unit through the time series. The Hamming distance [42], which denotes the minimum number of errors that

TABLE IV
NUMBER OF REFERENCE OBJECTS COLLECTED AT THE OBJECT LEVEL FOR ALL THE IMAGES (IS = IMPERVIOUS SURFACE, PS = PERVIOUS SURFACE)

Two-Stage Classification	Class	Image						
		2003	2005	2007	2010	2012	2015	2017
General urban land cover classification	Bright IS	378	417	421	332	245	445	447
	Dark IS	201	289	231	303	213	253	361
	Shadow	231	193	263	156	79	49	253
	Soil	424	202	214	62	117	79	262
	Vegetation	786	722	573	436	312	577	667
	Water	269	156	134	175	173	90	171
Shadow classification	Shaded IS	199	177	138	134	85	68	154
	Shaded PS	108	152	83	98	55	47	126

TABLE V
CONFUSION MATRIX AND ACCURACY ASSESSMENT FOR THE OBJECT-LEVEL CLASSIFICATION IN THE FIRST STAGE FOR THE REPRESENTATIVE IMAGE OF SHENZHEN 2003 (IS = IMPERVIOUS SURFACE, UA = USER'S ACCURACY, PA = PRODUCER'S ACCURACY, OA = OVERALL ACCURACY)

Classified Data	Reference Data							
	Bright IS	Dark IS	Shadow	Soil	Vegetation	Water	Total	UA (%)
Bright IS	184	2	0	3	0	0	189	97.35
Dark IS	1	98	0	2	0	1	102	96.07
Shadow	0	0	112	0	0	6	118	94.91
Soil	4	0	0	207	1	0	212	97.64
Vegetation	0	0	1	0	392	0	393	99.74
Water	0	0	2	0	0	127	129	98.44
Total	189	100	115	212	393	134	OA: 97.99	
PA (%)	97.35	98.00	97.39	97.64	99.74	94.77	Kappa: 0.97	

could have transformed one string into the other, was employed to measure the similarity between the detected change result and the reference change profile. A smaller Hamming distance indicates a higher accuracy. The aforementioned accuracy assessments from the two perspectives ensured the reliability of the continuous change detection results.

IV. RESULTS AND ANALYSIS

A. Impervious Surface Extraction

Table V shows the accuracy of the general urban land-cover classification for the representative image of 2003. The results show a satisfactory performance in terms of OA (97.99%) and kappa coefficient (0.97). In the meantime, some confusion can be found between the bright impervious surface/soil and dark impervious surface/water and shadow, due to their very similar spectral signatures, which is also the main challenge in land-cover classification from high-resolution images. A local area composed of complicated urban features is presented in Fig. 4(a) and (b) to further illustrate the result of the urban land-cover classification. In general, by visual inspection, it can be observed that most areas are correctly identified, wherein the large shadows caused by tall buildings, as a unique problem in impervious surface mapping from high-resolution images, can also be well recognized by the proposed method.

The general land-cover classification results indicate that the shadows account for a considerable amount of the total area. For instance, the detected shadows in the image of Shenzhen 2007 occupy approximately 14.9% of the entire image, and should not be ignored when dealing with impervious surface estimation. The accuracy of the shadow classification is shown in Table VI. The OA and the kappa coefficient are 97.30% and 0.93, respectively. Fig. 4(c) and (d) presents an example of shadow classification. It can be seen that the shaded areas are mainly roads (impervious surfaces) and urban greening (pervious surfaces). In Fig. 4(d), the impervious surfaces associated with roads are successfully recognized from the shaded areas, which can effectively avoid the underestimation of impervious surfaces caused by shadows.

The accuracy of the classification in two stages for all the images is shown in Fig. 5, and a representative impervious surface map is presented in Fig. 6. It can be concluded that the multiple features, integrating the spectral, spatial, and semantic information in the high-resolution images, have a great ability to comprehensively describe complicated urban land covers, and hence extract impervious surfaces from multitemporal high-resolution images with a promising accuracy, which provides a firm foundation for the subsequent analysis related to the characteristics of impervious surfaces.

B. Impervious Surface Change Between Neighboring Years

Based on the extracted impervious surface maps, a number of impervious surface changes at the grid level were detected in the Shenzhen central urban areas across the 15 years, and the accuracies of the change detection between neighboring years were assessed (see Table VII). In general, the change detection results show reasonable performance, with OAs ranging

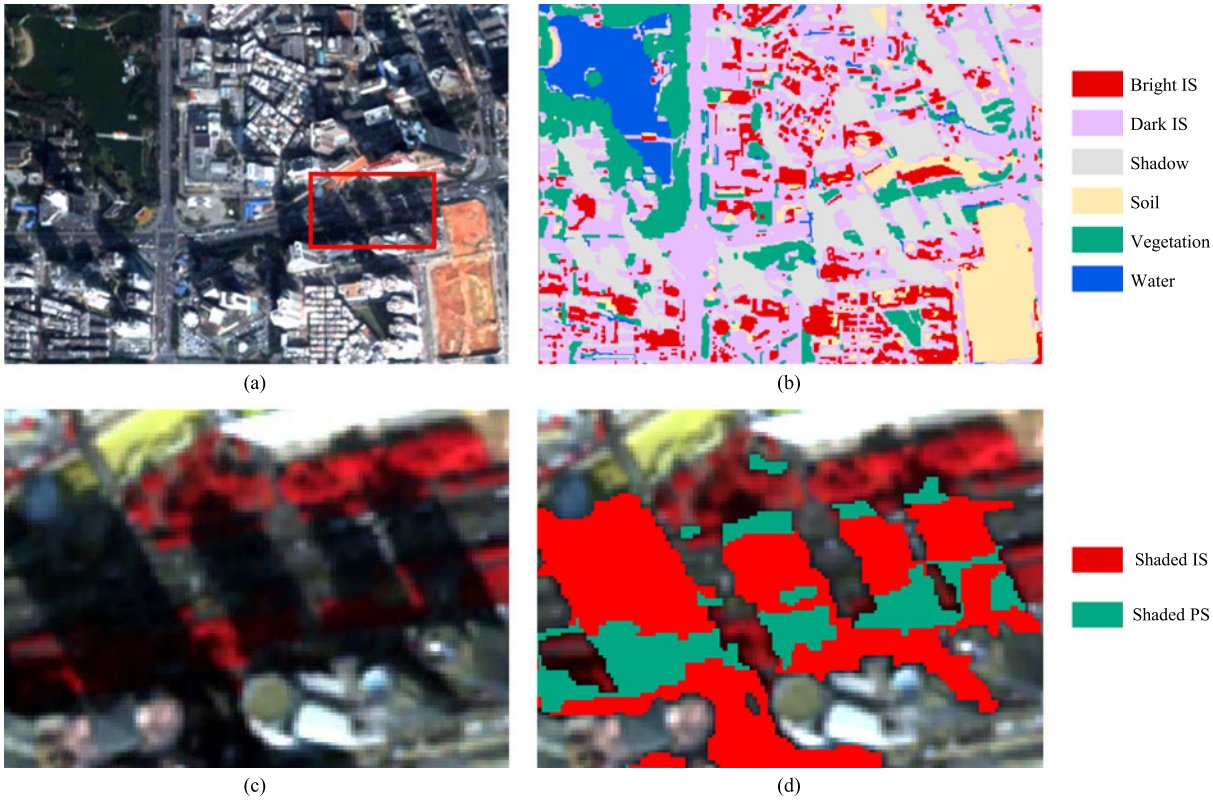

Fig. 4. Local examples of the classification results: (a) true-color image, (b) general urban land-cover classification, (c) false-color image, and (d) shadow classification. The red rectangular border in (a) corresponds to the image extent shown in (c) and (d).

TABLE VI
CONFUSION MATRIX AND ACCURACY ASSESSMENT FOR THE OBJECT-LEVEL CLASSIFICATION IN THE SECOND STAGE FOR THE REPRESENTATIVE IMAGE OF SHENZHEN 2003 (IS = IMPERVIOUS SURFACE, PS = PERVIOUS SURFACE, UA = USER'S ACCURACY, PA = PRODUCER'S ACCURACY, OA = OVERALL ACCURACY)

Classified data	Reference data			
	Shaded IS	Shaded PS	Total	UA (%)
Shaded IS	98	2	100	98
Shaded PS	2	46	48	95.83
Total	100	48	OA: 97.30	
PA (%)	98	95.83	Kappa: 0.93	

from 85.7% to 93.9% (average value: 89.1%) and the kappa coefficients varying from 0.65 to 0.86 (average value: 0.75). In addition to some misclassifications remaining in complicated and challenging areas, the major detection errors were caused by the viewing angle difference between the high-resolution time-series images. The significant difference of the viewing angles among the images, leading to building inclination toward different directions and target occlusion to varying degrees, can severely affect the change detection result. This issue is a great challenge with respect to change detection from high-resolution images in complex urban areas. In fact, the employed hot-spot change detection strategy can alleviate the viewing angle effect, to some extent, but the pixel-based method has difficulty in handling such a problem [4].

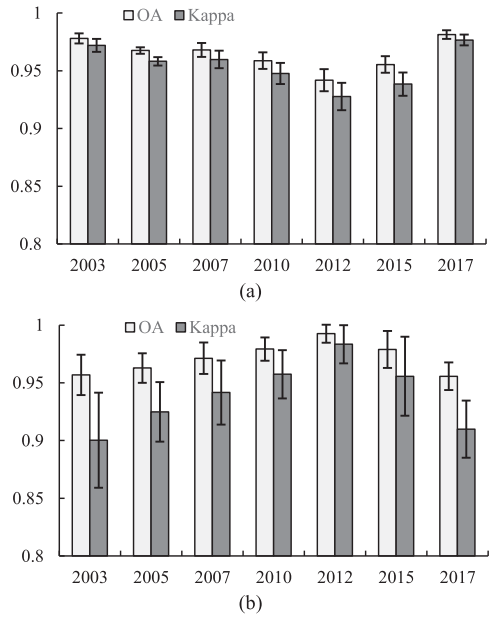

Fig. 5. Classification accuracy for all the images used in this study. (a) General urban land-cover classification. (b) Shadow classification (OA = overall accuracy).

A post-classification comparison was also conducted to reveal the detailed change trajectory of the impervious surfaces. In the detected changed areas, the land-cover class with the maximum change between neighboring years was regarded

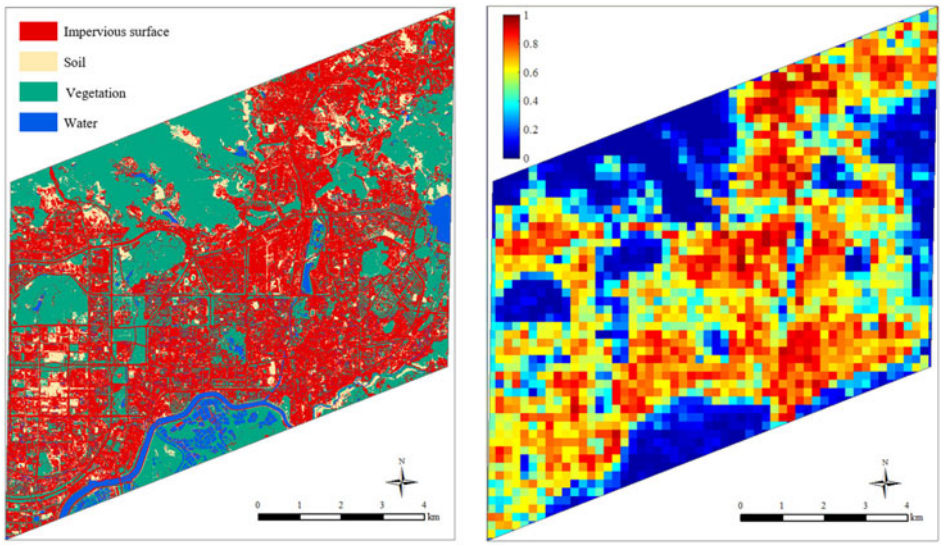

Fig. 6. (a) Final impervious surface map for a representative image of 2003. (b) Impervious surface percent map aggregated at 200 m in grid level for a representative image of 2003.

TABLE VII
CONFUSION MATRIX AND ACCURACY ASSESSMENT FOR THE GRID-LEVEL CHANGE DETECTION BETWEEN NEIGHBORING YEARS (OA = OVERALL ACCURACY)

	Detected	Reference			Detected	Reference	
		Changed	Unchanged			Changed	Unchanged
2003–2005	Changed	46	3	2010–2012	Changed	10	1
	Unchanged	8	90		Unchanged	1	21
	OA (%)	92.52			OA (%)	93.94	
	Kappa	0.83			Kappa	0.86	
2005–2007	Changed	16	5	2012–2015	Changed	22	13
	Unchanged	3	39		Unchanged	2	68
	OA (%)	87.30			OA (%)	85.71	
	Kappa	0.71			Kappa	0.65	
2007–2010	Changed	30	11	2015–2017	Changed	18	5
	Unchanged	5	77		Unchanged	3	43
	OA (%)	86.99			OA (%)	88.41	
	Kappa	0.70			Kappa	0.73	

TABLE VIII
ACCURACY OF THE IMPERVIOUS SURFACE CONVERSION

	Accuracy (#)	Accuracy (%)
2003–2005	44/46	95.6
2005–2007	13/16	81.2
2007–2010	28/30	93.3
2010–2012	9/10	90.0
2012–2015	20/22	90.9
2015–2017	17/18	94.4

as the main source of the impervious surface transition. For instance, when the proportion of the soil showed the largest change compared to other classes (i.e., water and vegetation) in a changed grid, we considered that, in this unit, the main conversion was from impervious surface to soil or from soil to impervious surface. Table VIII presents the accuracy of the impervious surface transition for the changed areas. The results show a relatively high correctness ranging from 81.2% to 95.6%, which indicates the high credibility of the detected impervious surface transformation. The proportion of each change trajectory related to impervious surfaces is shown in Table IX. For instance, during 2003–2005, 46 grids were detected as change scenes, in which 71.7% (33/46) of the grids showed the main land-cover transition from soil to impervious surface. In general, the most frequent change trajectory was from soil to impervious surface (43.7%), followed by the transitions from vegetation to impervious surface (24.6%), impervious surface to soil (18.3%), and impervious surface to vegetation (9.2%). In addition, transition from impervious surface to water and from water to impervious surface, were rarely found in the study area. Specifically, before 2010, the changed areas were mainly due to the conversion from soil or vegetation to impervious surface. These phenomena indicate that the city may have experienced a number of infrastructure constructions during this period. Then in 2010–2015, the impervious surface increase was nearly equal to the impervious surface loss in the detected changed areas. Finally,

TABLE IX
PERCENTAGES OF THE CHANGED TYPES FOR DETECTED CHANGED AREAS (IS = IMPERVIOUS SURFACE, VEG = VEGETATION)

	Soil to IS (%)	Veg to IS (%)	Water to IS (%)	IS to Soil (%)	IS to Veg (%)	IS to Water (%)
2003–2005	71.7	17.4	6.5	4.4	0	0
2005–2007	18.7	37.5	0	31.3	12.5	0
2007–2010	53.4	26.7	0	3.3	13.3	3.3
2010–2012	30	20	0	40	10	0
2012–2015	27.3	31.8	4.6	22.7	13.6	0
2015–2017	5.6	22.2	0	50	16.6	5.6
All	43.7	24.6	2.8	18.3	9.2	1.4

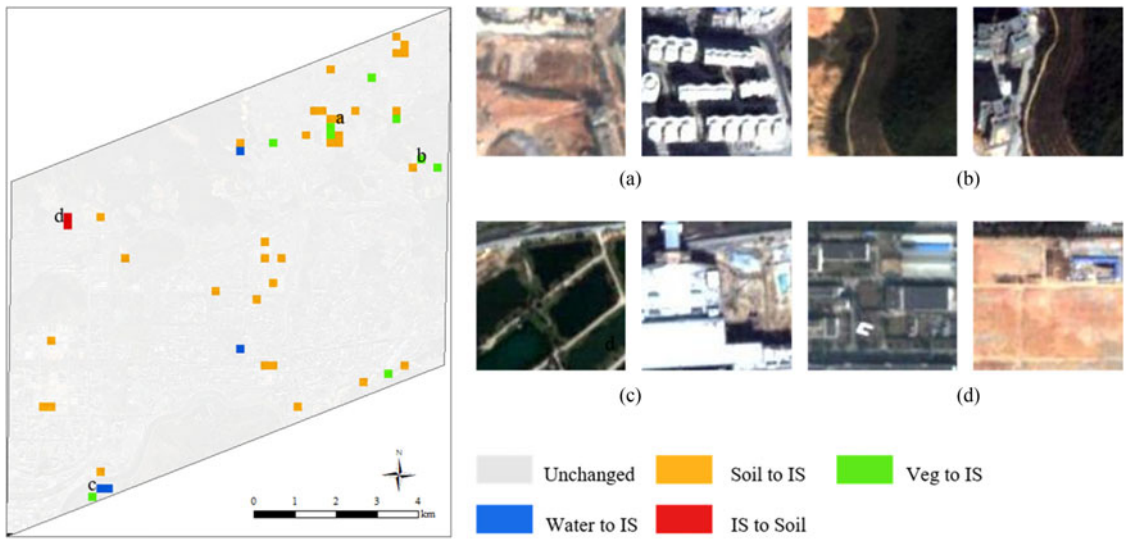

Fig. 7. Representative map of change transition from 2003 to 2005 with some local examples of the different change types (IS = impervious surface, Veg = vegetation).

in 2015–2017, half of the changed areas referred to the transition from impervious surface to soil, indicating that more building demolition activities may have taken place during this period. A typical example of the change transition between 2003 and 2005 is illustrated in Fig. 7. A variety of impervious surface change trajectories can be found due to the frequent building construction and demolition. The impervious surfaces can be transformed from soil, vegetation, and water and, in turn, the impervious surfaces can also be converted back to pervious surfaces such as soil.

C. Impervious Surface Change Patterns Across the Time Series

Apart from the impervious surface change between neighboring years, we also assessed the impervious surface change patterns across the time series to reveal the detailed characteristics of the impervious surfaces. The change profile of a monitoring unit (i.e., a grid) was represented by a long string consisting of 0 and 1, referring to the unchanged and changed years, respectively. Thus, a continuous change profile was composed of six change intervals (seven multitemporal images). In this study, the accuracy across the time series yielded a relatively small average Hamming distance of 0.32, which means that the error rate of the detected profile was 5.3% (0.32/6) compared to the reference change pattern. Furthermore, ∼76% of the total detected areas completely matched with the reference data. Overall, the accuracy of the impervious surface change profile across the time series is reasonable considering the great challenges (e.g., the large spatial heterogeneity and error propagation) in change detection from multitemporal images.

Fig. 8 illustrates the change detection result in the study area over the past 15 years. The timing of the changes is also provided. It is noteworthy that most of the detected areas changed only once over the past 15 years, but some areas changed multiple times. Some typical examples of the continuous change results are presented in Fig. 9, referring to the three main types of change across the time series. Fig. 9(a) and (b) shows the increase of impervious surfaces corresponding to building construction, in which soil and vegetation are converted to impervious surfaces during urban development. Fig. 9(c), (d), and (e) represents the loss of impervious surfaces, which mainly refers to building demolition. In addition to such single changes across the time series, some regions have changed more than once. In Fig. 9(f), the pervious surface (i.e., vegetation) was converted to impervious surface due to the construction of some temporary buildings in 2010, and then the impervious surface was transformed back to pervious surface (i.e., soil) following the

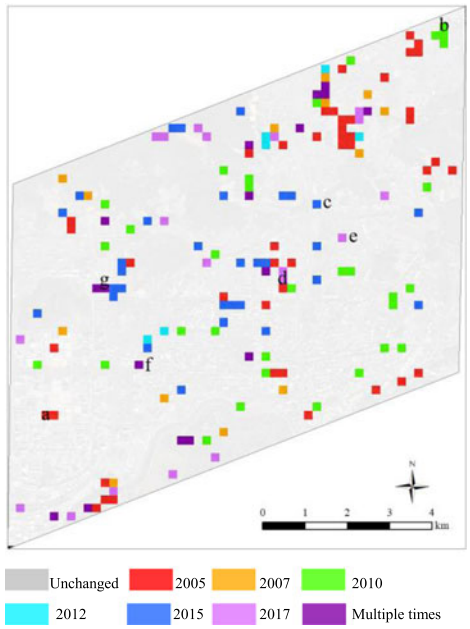

Fig. 8. Change detection result for the Shenzhen central areas over the past 15 years. The letters a–g represent the locations of some typical examples shown in Fig. 9.

demolition of the buildings in 2012. A similar repeated change can also be seen in Fig. 9(g). In 2012, the old buildings were dismantled and the impervious surface was converted back to soil, but in 2015, some new buildings were constructed at the same location and the soil was transformed to impervious surface. It should be noted that the studies using medium-resolution images (e.g., Landsat) usually focus on the urban expansion at a macro level, with the assumption that the urban development is irreversible. The impervious surface converted back to pervious surface is often regarded as an illogical class transition [3], [5], [7]. However, this assumption makes it impossible to capture the subtle changes of impervious surfaces within urban areas [4]. Hence, time series of high-resolution images are necessary for the monitoring of impervious surfaces and can help us to assess the details (e.g., location, type, and frequency) of the impervious surface changes within urban areas, providing insights into the drivers of change and urban development.

D. Urban Land-Use and Development Policy Evolution

China has experienced rapid urbanization since the initiation of the "reform and opening-up" policy in late 1978. By the end of 2011, the urban population exceeded that of rural dwellers, and 51% of the total population lived in urban areas [22]. A large number of land-cover and land-use changes have occurred during the process of urban development. With the rapid urban–rural transformation, various issues have arisen, e.g., excessive consumption of resources, low-efficiency land use, and environmental pollution, giving rise to the need for new policies for urban sustainable development [43]. In recent years, the Chinese government has paid much more attention to protecting the urban environment, promoting ecosystem services, and improving land-use efficiency. Such urban development policy evolution can also be seen in Shenzhen. Fig. 10 presents the impervious surface composition in Shenzhen over the past 15 years. The piecewise linear fitting model was used to quantitatively analyze the overall change tendency of the impervious surfaces, and the year of 2012 was regarded as a turning point. Compared to the result using a continuous fitting line without breakpoint (R^2: 0.03), the piecewise linear fitting achieves a better performance (R^2: 0.90) in describing the trend of impervious surface change. The result in Fig. 10 indicates that the impervious surfaces gradually increased before 2012 (0.82% per year) and then showed a decreasing tendency (1.46% per year). These phenomena of impervious surface change could also provide clues for the adjustment of land-use policy by the Shenzhen government during the process of urban development.

Specifically, from 2003 to 2012, the urban function and infrastructure was gradually improved and perfected, e.g., the construction of the Shenzhen Convention and Exhibition Center, as shown in Fig. 9(a). In the meantime, with the increase of the floating population and the demand for housing, the real estate industry boomed and became one of the main drivers for rapid urbanization [e.g., Fig. 9(b)]. However, the local government noticed that the socio-economic development had exceeded the sustainable supply capacity of resources [43] and, hence, started to change land-use policy to further improve urban competitiveness. One strategy was the promotion of urban ecosystem services [8], e.g., land-cover changes from continuous urban fabric toward green spaces. In a government document released in 2012 [44], the Shenzhen government pledged to strengthen ecological conservation in the city. It is believed that urban green spaces play an important role for the local environment, public health, and balance of the city ecosystem [45]. Hence, in the process of urban development, it is found that some impervious surface areas are converted back to vegetation, becoming more environmentally friendly and improving the urban ecological function [e.g., Fig. 9(c)]. In addition, urban renewal is another approach to urban sustainable development. In 2012, the city managers enacted detailed measures for urban renewal planning, mainly referring to the activities of demolition and the reconstruction of buildings, regeneration of the old industrial areas, and urban functional changes [46]. The redevelopment of old and inefficient built-up areas inside the cities can create a better living environment, enhance land-use efficiency, and promote sustainable development. For instance, over the past 30 years, many villages in the urban fringe have been engulfed by the ever-expanding urban areas and have become the informal settlements known as "urban villages", which are characterized by extremely high density buildings and substandard living conditions [23], [47]. Since Shenzhen has grown at an amazing speed from a small fishing village to a modern megacity, the urban built-up areas are dotted with many urban villages covering large areas. Many migrant workers reside in the urban villages as they cannot afford the high rent in other formal settlements. However, urban villages lack reliable medical and health services, adequate public spaces, complete urban facilities, and other basic services, and have become a complicated socio-economic problem in urban sustainable development [23]. The

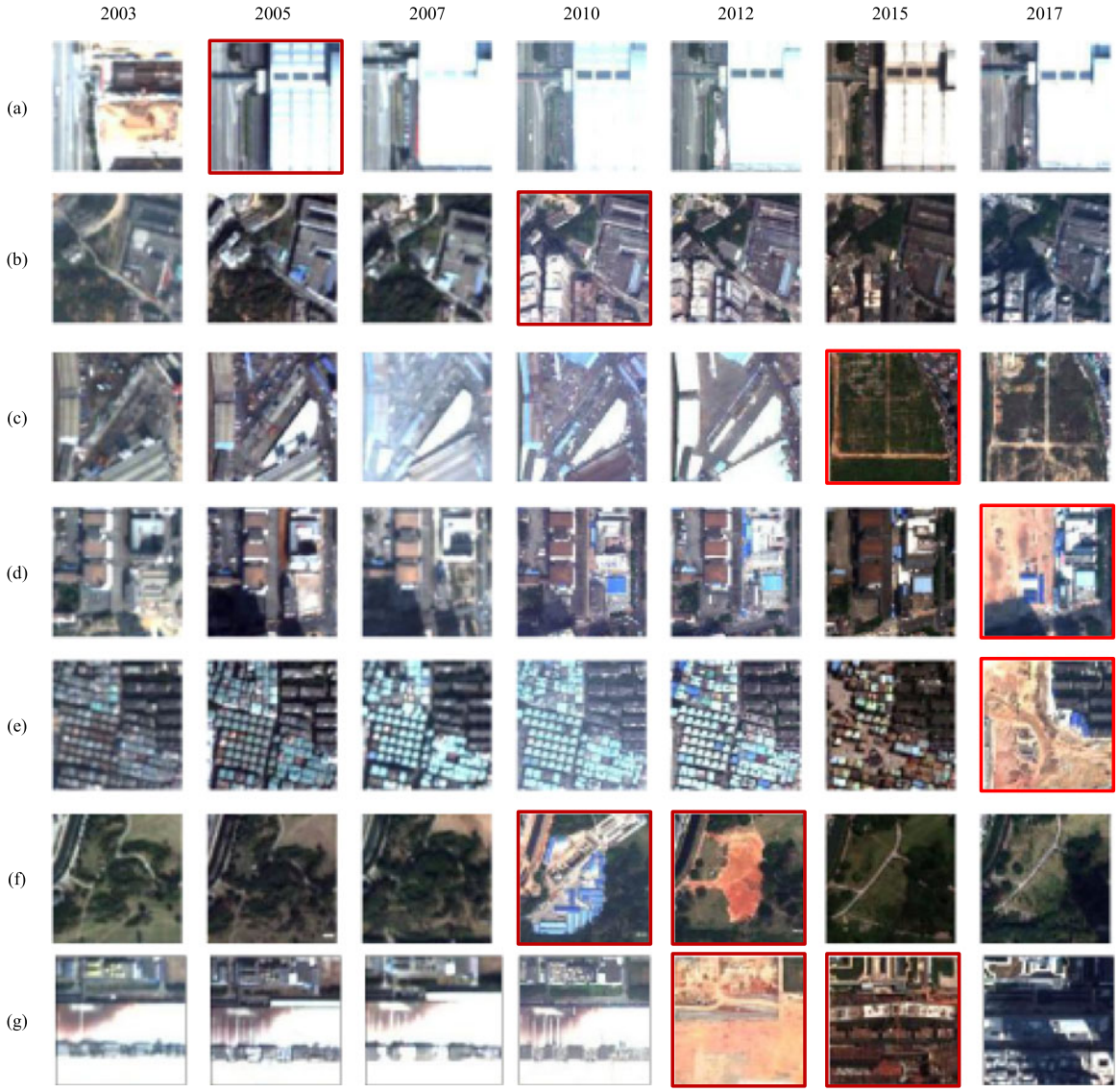

Fig. 9. Some typical examples of impervious surface change profiles, where the images with red borders represent a change compared to a previous date. The spatial locations of the examples are labeled in Fig. 8.

latest Shenzhen 13th Five-Year Plan announced in 2016 [48] pledged that the city would further promote the urban renewal policy to improve the city's service quality. During the implementation of the urban redevelopment plan, the urban villages will be gradually dismantled and the land will serve other useful purposes [e.g., Fig. 9(e)]. Demolition and reconstruction in industrial areas, e.g., old industrial areas replaced by high-rise residential buildings [see Fig. 9(g)], is also among the measures of the urban renewal plan. These activities associated with urban redevelopment will result in urban functional changes, facilitating proper and efficient land use for urban sustainable development.

E. Landscape Change Analysis

Fig. 11 presents the landscape change of the impervious surfaces in Shenzhen over the past 15 years. Piecewise linear fitting was again used to analyze the general landscape change of the impervious surfaces. From 2003 to 2012, the rising tendency of LPI (1.03% per year) and MPA (0.01 hectare/year) indicate that the impervious surface patches became more dominant and connected, resulting from the construction of new buildings [e.g., Fig. 9(a), and (b)]. In the meantime, the larger LPI and MPA resulted in descending PD (2.91# per year), indicating increased spatial homogeneity of the impervious surface patches. Subsequently, from 2012 to 2017, opposite trends for all the metrics can be observed (i.e., the decreasing trend of LPI (2.28% per year) and MPA (0.03 hectare per year) and the increasing tendency of PD (6.52# per year), indicating that the impervious surface patches became more fragmented during this period. These phenomena can be attributed to the fact that the demolition of some old buildings reduced the cohesion of the impervious surface patches [e.g., Fig. 9(d)]. In summary, the changes of these landscape metrics provide us with clues on the

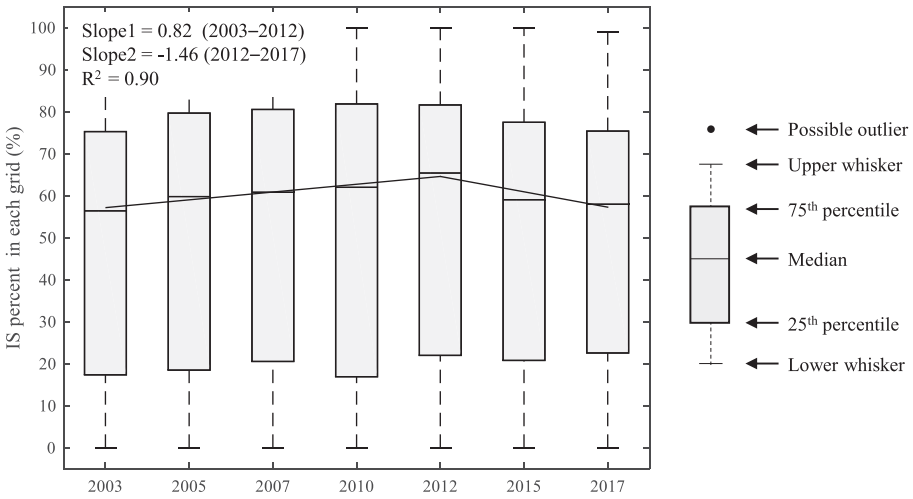

Fig. 10. Boxplot and trend line showing the IS percentage spanning 15 years in Shenzhen (IS = impervious surface). The vertical axis represents the distribution of the impervious surface percentage value computed at each grid.

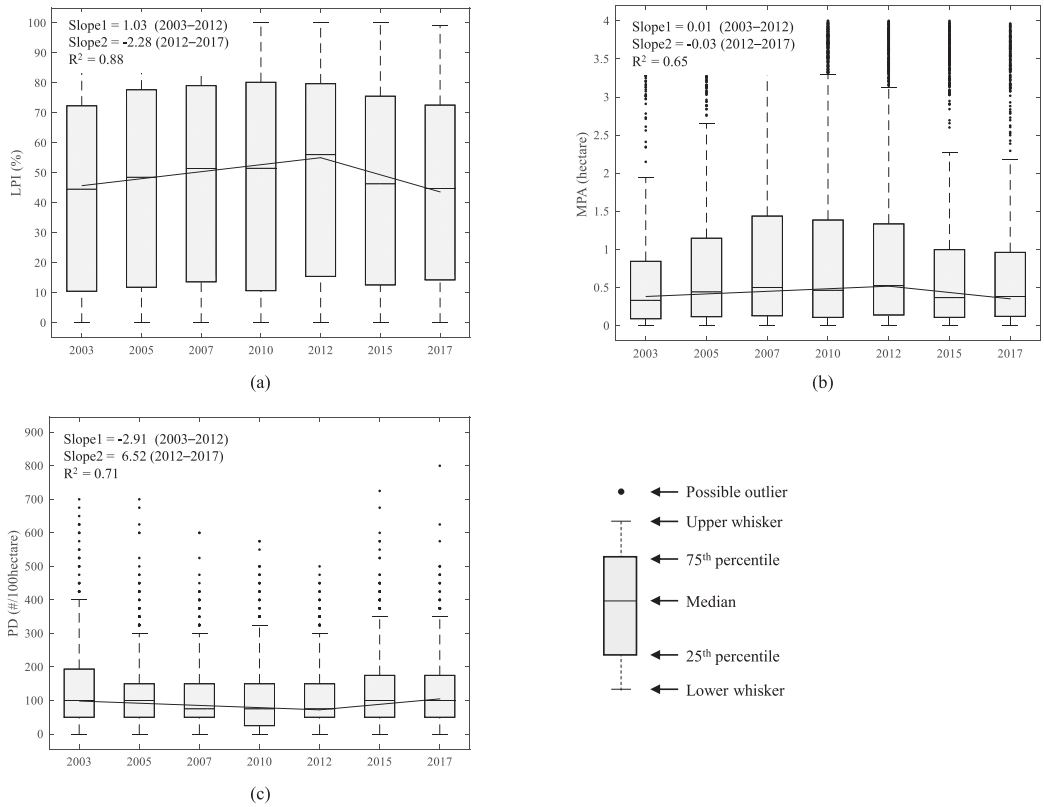

Fig. 11. Boxplots and trend lines of the landscape metrics. (a) Largest patch index. (b) Mean patch area. (c) Patch density. The vertical axis represents the distribution of the landscape metric computed at each grid.

urban development patterns of Shenzhen over the past 15 years, and the change tendency is similar to the previous analysis in Section IV-D. Before 2012, Shenzhen mainly experienced infrastructure construction, with increasing impervious surfaces in terms of the larger LPI and MPA but, subsequently, the impervious surfaces showed a decreasing tendency, reflecting the adjusted strategies for urban development after 2012 (e.g., the promotion of urban ecosystem services and the implementation of the urban renewal plan).

V. Discussions

A. Feature Importance

In this section, the importance and relevance of the features are analyzed. Using the RF model, the feature contribution can be quantified by randomly permuting the values of the out-of-bag samples (OOB, the unchosen samples for training a decision tree) for a certain variable. The average decrease in accuracy over all the trees, caused by the feature permutation, is regarded

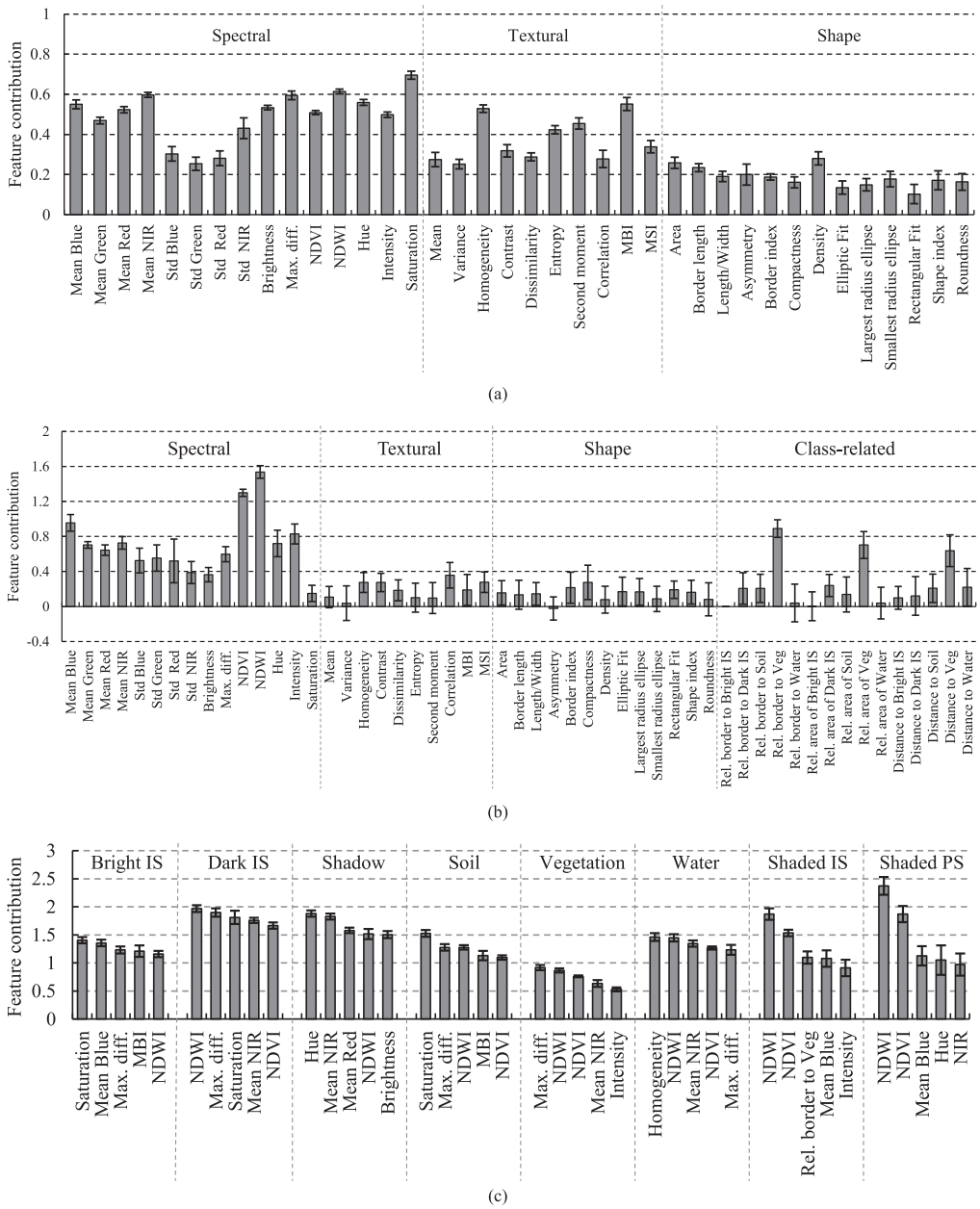

Fig. 12. (a) Feature contribution in general urban land-cover classification. (b) Feature contribution in shadow classification. (c) The most relevant features (top five) for individual classes.

as the feature importance. The normalized importance can then be obtained by dividing each feature importance by its standard deviation [49].

Fig. 12 shows the feature contributions to the overall classification result. The detailed feature description can be found in Table II. In urban land-cover classification, all the features present a positive contribution to the classification. The spectral features show the highest contribution, followed by the textural features and shape features [see Fig. 12(a)]. A similar trend can be found with regard to shadow classification in Fig. 12(b). In addition, in the class-related feature set, the features associated with vegetation make a greater contribution.

The top five features that are the most relevant for the individual classes are shown in Fig. 12(c). This provides the hint that NDWI plays a very important role in identifying all classes, probably due to the fact that NDWI is not only a water index, but it also shows higher responses in other low-albedo surfaces, e.g., shadow and dark impervious surfaces [50]. NDVI, a commonly used vegetation index, is another very important feature in the discrimination of most classes such as vegetation and detailed shaded land cover. The hue-saturation-intensity (HSI) components are also very effective in the identification of classes such as shadow and soil, which has been reported in [51] and [52]. MBI shows a relatively high contribution to bright impervious surface classification since MBI mainly represents the buildings with high reflectance [29]. The *Homogeneity* texture shows the most relevance for water identification due to the fact that water is homogeneous, with low variance. Finally, the relative

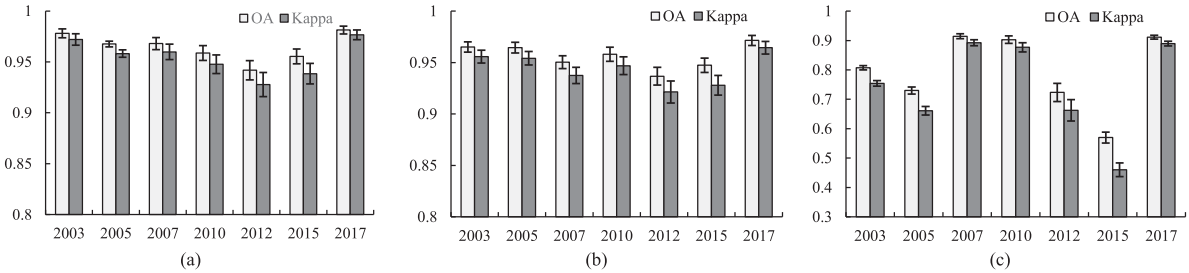

Fig. 13. Accuracies of different strategies of training sample collection. (a) Collecting training samples and performing classification separately for each image. (b) Collecting training samples from the whole data set and building a single classification model. (c) Transfer training sample collection.

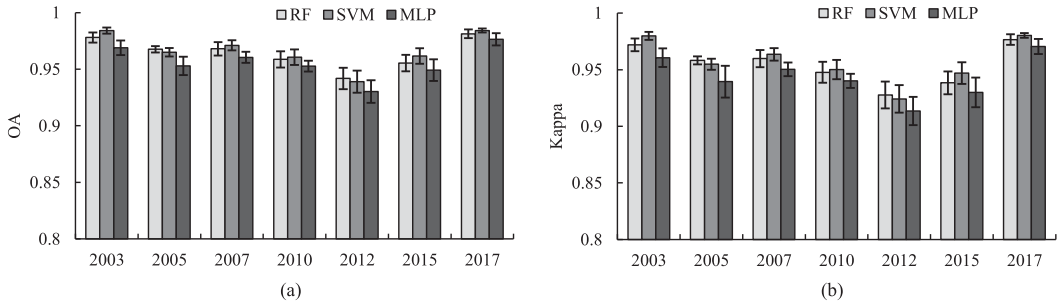

Fig. 14. Accuracies of different classifiers for urban land-cover classification. (a) Overall accuracy (OA). (b) Kappa.

border to vegetation presents a relatively high contribution to the discrimination in shaded areas. The shaded areas are mainly roads and green belts, and hence the spatial relationship with vegetation can assist to detailed shadow classification.

Summing up, most of the features make a positive contribution to the overall classification, and the most relevant features for the individual classes come from different feature categories. More importantly, in most cases, it seems very difficult to select one optimal feature set for different objects and scenes, due to the complex landscape characteristics of the study area. Therefore, in this study, we employed multiple features (spectral, textural, shape, and class-related features) to represent the complex image scenes from different perspectives, in order to produce an accurate classification result for the subsequent time-series analysis.

B. Training Sample Collection Across Time Series

In our study, the classification was performed separately for each year. In this section, we considered two other options for training sample collection across the time series.

First, we collected training samples from all the images to build a single classification model to classify the whole data set. Due to the difference in the spectral resolution of the images, the spectral features corresponding to the same four spectral bands (i.e., blue, green, red, and near infrared band) were used in this experiment. The accuracy is shown in Fig. 13(b), where it can be seen that using training samples across all the images to build a single classification model also achieves a reasonable performance, but is inferior to the separate classification for each image [see Fig. 13(a)]. We then further investigated the possibility of transfer training across the time series. For instance, to perform the classification of Shenzhen 2003, the training samples were obtained from the other six multitemporal images. The accuracy is shown in Fig. 13(c). Although the transfer training has the potential to reduce the cost of training sample collection, the classification accuracy is not fully satisfactory for the subsequent change analysis. Therefore, in our study, we performed the classification separately to obtain an accurate result, guaranteeing a reliable time-series analysis.

C. Comparison of Different Classifiers

In this section, we considered two other classifiers—support vector machine (SVM) and multilayer perceptron (MLP) neural network—using the same training and validation datasets to test their performance in urban land-cover classification. SVM was implemented by the use of a Gaussian radial basis function (RBF) kernel. The penalty parameter and the bandwidth of the RBF kernel were selected by tenfold cross-validation [47]. MLP is one of the most widely used artificial neural networks. The input layer corresponds to the multiple features used in classification, and the output layer represents the different kinds of land covers. A single hidden layer was used in this study since it is sufficient for most classification tasks [53]. The number of nodes in the hidden layer can be estimated as follows [54]:

$$N_h = \mathrm{INT}\sqrt{N_i \times N_o} \tag{5}$$

where N_h denotes the number of nodes in the hidden layer, N_i is the number of nodes in the input layer, and N_o is the number of nodes in the output layer. A back-propagation algorithm was used to adjust the weights and minimize the overall error. Finally, different parameters (e.g., learning rate, and momentum factor) were tested and selected through the learning process [54].

The accuracies of the different classifiers for urban land-cover classification are shown in Fig. 14. It can be seen that all the classifiers achieve accuracies that are very close to each other. In this study, we considered that RF has some advantages, such

as easy parameterization and convenient evaluation for feature importance [33]. In these regards, RF was selected as a suitable classifier for our research into urban land-cover classification and time-series analysis.

VI. Conclusion

Impervious surfaces are recognized as a major indicator of urban development and environmental quality. In recent years, many cities in China have undergone rapid urbanization, with frequent subtle changes related to impervious surfaces resulting from infrastructure construction. Such change information is very important for urban planning and environmental assessment. In this study, we assessed the change of impervious surfaces using time series of high-resolution images. The method was applied to multitemporal images of Shenzhen, a typical megacity in China, at ∼2-year intervals from 2003 to 2017. Some general conclusions can be summarized as follows:

1) We developed an object-based classification method integrating multiple features, including spectral, textural, shape, and class-related features, which can make full use of the information inherent in high-resolution data to deal with the land-cover confusion and shadow problems, producing accurate impervious surface maps to guarantee reliable impervious surface change detection.
2) The details of the impervious surface changes (e.g., location, type, and frequency) were investigated using the time series of high-resolution data. The increase of impervious surfaces mainly refers to building construction, and the decrease of impervious surfaces usually corresponds to building demolition. It is also revealed that impervious surfaces can be converted back to pervious surfaces, and some regions have changed more than once due to urban redevelopment. These phenomena are impossible to detect with the traditional assumption of irreversible urban transition. Our results demonstrate that high-resolution images are essential for the precise monitoring of impervious surfaces.
3) We found that impervious surfaces in Shenzhen gradually increased before 2012, but subsequently showed a decreasing tendency, reflecting the adjusted strategies for urban development. It was demonstrated that high-resolution images can provide insights into the urban development patterns during the process of urbanization.

Acknowledgment

The authors would like to thank the anonymous reviewers for the insightful and constructive suggestions, which significantly improved the quality of this paper.

References

[1] Q. Weng, "Remote sensing of impervious surfaces in the urban areas: Requirements, methods, and trends," *Remote Sens. Environ.*, vol. 117, pp. 34–49, Feb. 2012.
[2] C. Cai, P. Li, and H. Jin, "Extraction of Urban impervious surface using two-season worldview-2 images: A comparison," *Photogramm. Eng. Remote Sen.*, vol. 82, no. 5, pp. 335–349, May 2016.
[3] L. Zhang and Q. Weng, "Annual dynamics of impervious surface in the Pearl River Delta, China, from 1988 to 2013, using time series Landsat imagery," *ISPRS J. Photogramm. Remote Sens.*, vol. 113, pp. 86–96, Mar. 2016.
[4] X. Huang, D. Wen, J. Li, and R. Qin, "Multi-level monitoring of subtle urban changes for the megacities of China using high-resolution multi-view satellite imagery," *Remote Sens. Environ.*, vol. 196, pp. 56–75, Jul. 2017.
[5] X.-P. Song, J. O. Sexton, C. Huang, S. Channan, and J. R. Townshend, "Characterizing the magnitude, timing and duration of urban growth from time series of Landsat-based estimates of impervious cover," *Remote Sens. Environ.*, vol. 175, pp. 1–13, Mar. 2016.
[6] C. Wu, C. Deng, and X. Jia, "Spatially constrained multiple endmember spectral mixture analysis for quantifying subpixel Urban impervious surfaces," *IEEE J. Sel. Topics Appl. Earth Observ. Remote Sens.*, vol. 7, no. 7, pp. 1976–1984, Jun. 2017.
[7] X. Li, P. Gong, and L. Liang, "A 30-year (1984–2013) record of annual urban dynamics of Beijing City derived from Landsat data," *Remote Sens. Environ.*, vol. 166, pp. 78–90, Sep. 2015.
[8] J. Haas and Y. Ban, "Mapping and monitoring urban ecosystem services using multitemporal high-resolution satellite data," *IEEE J. Sel. Topics Appl. Earth Observ. Remote Sens.*, vol. 10, no. 2, pp. 669–680, Feb. 2017.
[9] H. W. Zheng, G. Q. Shen, and H. Wang, "A review of recent studies on sustainable urban renewal," *Habitat Int*., vol. 41, pp. 272–279, Jan. 2014.
[10] Y. Feng, D. Lu, E. F. Moran, L. V. Dutra, M. F. Calvi, and M. A. F. de Oliveira, "Examining spatial distribution and dynamic change of urban land covers in the Brazilian amazon using multitemporal multisensor high spatial resolution satellite imagery," *Remote Sens*., vol. 9, no. 4, pp. 381–400, Apr. 2017.
[11] D. Wen, X. Huang, L. Zhang, and J. A. Benediktsson, "A novel automatic change detection method for urban high-resolution remotely sensed imagery based on multiindex scene representation," *IEEE Trans. Geosci. Remote Sens.*, vol. 54, no. 1, pp. 609–625, Jan. 2016.
[12] M. Volpi, D. Tuia, F. Bovolo, M. Kanevski, and L. Bruzzone, "Supervised change detection in VHR images using contextual information and support vector machines," *Int. J. Appl. Earth Obs.*, vol. 20, pp. 77–85, Feb. 2013.
[13] M. Hussain, D. Chen, A. Cheng, H. Wei, and D. Stanley, "Change detection from remotely sensed images: From pixel-based to object-based approaches," *ISPRS J. Photogramm. Remote Sens.*, vol. 80, pp. 91–106, Jun. 2013.
[14] L. Ma *et al.*, "Object-based change detection in Urban areas: The effects of segmentation strategy, scale, and feature space on unsupervised methods," *Remote Sens*., vol. 8, no. 9, pp. 761–778, Sep. 2016.
[15] F. Pacifici and F. Del Frate, "Automatic change detection in very high resolution images with pulse-coupled neural networks," *IEEE Geosci. Remote Sens. Lett.*, vol. 7, no. 1, pp. 58–62, Jan. 2010.
[16] C. Pratola, F. Del Frate, G. Schiavon, and D. Solimini, "Toward fully automatic detection of changes in suburban areas from VHR SAR images by combining multiple neural-network models," *IEEE Trans. Geosci. Remote Sens.*, vol. 51, no. 4, pp. 2055–2066, Apr. 2013.
[17] X. Zhang, P. Xiao, and X. Feng, "Impervious surface extraction from high-resolution satellite image using pixel-and object-based hybrid analysis," *Int. J. Remote Sens.*, vol. 34, no. 12, pp. 4449–4465, Mar. 2013.
[18] T. Blaschke, "Object based image analysis for remote sensing," *ISPRS J. Photogramm. Remote Sens.*, vol. 65, no. 1, pp. 2–16, Jan. 2010.
[19] S. W. Myint, P. Gober, A. Brazel, S. Grossman-Clarke, and Q. Weng, "Per-pixel vs. object-based classification of urban land cover extraction using high spatial resolution imagery," *Remote Sens. Environ.*, vol. 115, no. 5, pp. 1145–1161, May 2011.
[20] D. Lu and Q. Weng, "Extraction of urban impervious surfaces from an IKONOS image," *Int. J. Remote Sens.*, vol. 30, no. 5, pp. 1297–1311, Apr. 2009.
[21] P. Li, J. Guo, B. Song, and X. Xiao, "A multilevel hierarchical image segmentation method for urban impervious surface mapping using very high resolution imagery," *IEEE J. Sel. Topics Appl. Earth Observ. Remote Sens.*, vol. 4, no. 1, pp. 103–116, Mar. 2011.
[22] Yearbook, "China statistical yearbook," in *National Bureau of Statistics of China*. Beijing, China: China Statistics Press, 2012.
[23] X. Huang, H. Liu, and L. Zhang, "Spatiotemporal detection and analysis of Urban villages in mega city regions of China using high-resolution remotely sensed imagery," *IEEE Trans. Geosci. Remote Sens.*, vol. 53, no. 7, pp. 3639–3657, Jul. 2015.
[24] F. Module. (2009). *Atmospheric Correction Module: QUAC and FLAASH User's Guide*. [Online]. Available: http://www.harrisgeospatial.com/portals/0/pdfs/envi/flaash_module.pdf

[25] Y. Zhang, H. Zhang, and H. Lin, "Improving the impervious surface estimation with combined use of optical and SAR remote sensing images," *Remote Sens. Environ.*, vol. 141, pp. 155–167, Feb. 2014.
[26] W. Zhou, G. Huang, A. Troy, and M. L. Cadenasso, "Object-based land cover classification of shaded areas in high spatial resolution imagery of urban areas: A comparison study," *Remote Sens. Environ.*, vol. 113, no. 8, pp. 1769–1777, Aug. 2009.
[27] A. G. Definiens, *Definiens eCognition Developer 8 User Guide*. Munchen, Germany: Definens AG, 2009.
[28] R. M. Haralick, "Statistical and structural approaches to texture," *Proc. IEEE* vol. 67, no. 5, pp. 786–804, May 1979.
[29] X. Huang and L. Zhang, "Morphological building/shadow index for building extraction from high-resolution imagery over urban areas," *IEEE J. Sel. Topics Appl. Earth Observ. Remote Sens.*, vol. 5, no. 1, pp. 161–172, Feb. 2012.
[30] X. Huang, X. Liu, and L. Zhang, "A multichannel gray level co-occurrence matrix for multi/hyperspectral image texture representation," *Remote Sens.*, vol. 6, pp. 8424–8445, Sep. 2014.
[31] M. Wurm, H. Taubenböck, M. Weigand, and A. Schmitt, "Slum mapping in polarimetric SAR data using spatial features," *Remote Sens. Environ.*, vol. 194, pp. 190–204, Jun. 2017.
[32] J. Stefanski, B. Mack, and B. R. Waske, "Optimization of Object-Based Image Analysis With Random Forests for Land Cover Mapping," *IEEE J. Sel. Topics Appl. Earth Observ. Remote Sens.*, vol. 6, no. 6, pp. 2492–2504, Dec. 2013.
[33] C. Pelletier, S. Valero, J. Inglada, N. Champion, and G. Dedieu, "Assessing the robustness of Random Forests to map land cover with high resolution satellite image time series over large areas," *Remote Sens. Environ.*, vol. 187, pp. 156–168, Dec. 2016.
[34] P. Xiao, X. Zhang, D. Wang, M. Yuan, X. Feng, and M. Kelly, "Change detection of built-up land: A framework of combining pixel-based detection and object-based recognition," *ISPRS J. Photogramm. Remote Sens.*, vol. 119, pp. 402–414, Sep. 2016.
[35] T. Pham-Gia and T. L. Hung, "The mean and median absolute deviations," *Math. Comput. Model.*, vol. 34, no. 7/8, pp. 921–936, Oct. 2001.
[36] X.-P. Song, C. Huang, J. O. Sexton, S. Channan, and J. R. Townshend, "Annual detection of forest cover loss using time series satellite measurements of percent tree cover," *Remote Sens.*, vol. 6, no. 9, pp. 8878–8903, Sep. 2014.
[37] C. Leys, C. Ley, O. Klein, P. Bernard, and L. Licata, "Detecting outliers: Do not use standard deviation around the mean, use absolute deviation around the median," *J. Exp. Soc. Psychol.*, vol. 49, no. 4, pp. 764–766, Jul. 2013.
[38] J. Miller, "Short report: Reaction time analysis with outlier exclusion: Bias varies with sample size," *Quart. J. Exp. Psychol.*, vol. 43, no. 4, pp. 907–912, Apr. 1991.
[39] K. McGarigal, S. A. Cushman, M. C. Neel, and E. Ene, *FRAGSTATS: Spatial Pattern Analysis Program for Categorical Maps*, 2002. [Online]. Available: www.umass.edu/landeco/research/fragstats/fragstats.html
[40] S. Bernard, L. Heutte, and S. Adam, "On the selection of decision trees in random forests," in *Proc. Int. Joint Conf. Neural Netw.*, Atlanta, GA, USA, 2009, pp. 302–307.
[41] R. G. Congalton, "A review of assessing the accuracy of classifications of remotely sensed data," *Remote Sens. Environ.*, vol. 37, no. 1, pp. 35–46, Jul. 1991.
[42] R. Smarandache and P. O. Vontobel, "Quasi-cyclic LDPC codes: Influence of proto-and Tanner-graph structure on minimum Hamming distance upper bounds," *IEEE Trans. Inf. Theory*, vol. 58, no. 2, pp. 585–607, Feb. 2012.
[43] J. Qian, Y. Peng, C. Luo, C. Wu, and Q. Du, "Urban land expansion and sustainable land use policy in Shenzhen: A case study of China's rapid urbanization," *Sustainability*, vol. 8, no. 1, pp. 1–16, Dec. 2015.
[44] Shenzhen Government Online, *The Government Work Report,* 2012a. [Online]. Available: http://www.sz.gov.cn/zfgb/2012_1/gb797/201207/t20120724_1953350.htm. Accessed on: July 8, 2017.
[45] M. Lazzarini, P. R. Marpu, and H. Ghedira, "Temperature-land cover interactions: The inversion of urban heat island phenomenon in desert city areas," *Remote Sens. Environ.*, vol. 130, pp. 136–152, Mar. 2013.
[46] Shenzhen Government Online, *The Government Work Report.* 2012b. [Online]. Available: http://www.sz.gov.cn/zfgb/2012_1/gb774/201202/t20120208_1802813.htm. Accessed on: July 8, 2017.
[47] T. Zhang, X. Huang, D. Wen, and J. Li, "Urban building density estimation from high-resolution imagery using multiple features and support vector regression," *IEEE J. Sel. Topics Appl. Earth Observ. Remote Sens.*, vol. 10, no. 7, pp. 3265–3280, Jul. 2017.
[48] Shenzhen Municipality, *Shenzhen 13th Five-Year Plan for Urban Renewal*, 2016. [Online]. Available online: http://www.szpl.gov.cn/xxgk/ztzl/csgx135/. Accessed on July 8, 2017.
[49] N. Longbotham, C. Chaapel, L. Bleiler, C. Padwick, W. J. Emery, and F. Pacifici, "Very high resolution multiangle urban classification analysis," *IEEE Trans. Geosci. Remote Sens.*, vol. 50, pp. 1155–1170, Apr. 2012.
[50] G. Sun, X. Chen, X. Jia, Y. Yao, and Z. Wang, "Combinational build-up index (CBI) for effective impervious surface mapping in Urban Areas," *IEEE J. Sel. Topics Appl. Earth Observ. Remote Sens.*, vol. 9, pp. 2081–2092, May 2016.
[51] J. Liu, T. Fang, and D. Li, "Shadow detection in remotely sensed images based on self-adaptive feature selection," *IEEE Trans. Geosci. Remote Sens.*, vol. 49, pp. 5092–5103, Dec. 2011.
[52] G. Pan, F.-m. Li, and G.-j. Sun, "Digital camera based measurement of crop cover for wheat yield prediction," in *Proc. 2007 IEEE Int. Geosci. Remote Sensing Symp*. Barcelona, Spain, 2007, pp. 797–800.
[53] H. Zhang, Y. Zhang, and H. Lin, "A comparison study of impervious surfaces estimation using optical and SAR remote sensing images," *Int. J. Appl. Earth Obs.*, vol. 18, pp. 148–156, Aug. 2012.
[54] Q. Weng and X. Hu, "Medium spatial resolution satellite imagery for estimating and mapping urban impervious surfaces using LSMA and ANN," *IEEE Trans. Geosci. Remote Sens.*, vol. 46, pp. 2397–2406, Aug. 2008.

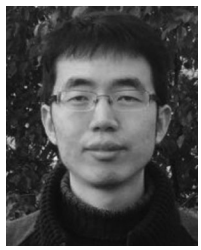

Tao Zhang received the B.S. degree in surveying and mapping from the Central South University, Changsha, China, in 2014. He is currently working toward the Ph.D. degree in photogrammetry and remote sensing from the State Key Laboratory of Information Engineering in Surveying, Mapping, and Remote Sensing, Wuhan University, Wuhan, China.

His current research interests include high-resolution image processing, and remote sensing applications.

Xin Huang (M'13–SM'14) received the Ph.D. degree in photogrammetry and remote sensing from Wuhan University, Wuhan, China, in 2009.

He is currently with the State Key Laboratory of Information Engineering in Surveying, Mapping, and Remote Sensing (LIESMARS), Wuhan University. He is currently a Luojia Distinguished Professor of Wuhan University, where he is engaged in remote sensing, photogrammetry, image interpretation, etc. He is the Founder and Director of the Institute of Remote Sensing Information Processing (IRSIP), School of Remote Sensing and Information Engineering, Wuhan University. He has authored or coauthored more than 110 peer-reviewed articles (SCI papers) in the international journals. He is the Lead Guest Editor of the special issue on Sparsity-Driven High Dimensional Remote Sensing Image Processing and Analysis for the *Journal of Applied Remote Sensing* (vol. 10, no. 4, Oct. 2016). Since 2016, he is an Associate Editor of the *Photogrammetric Engineering and Remote Sensing* (PE&RS). His current research interests include remote sensing image processing methods and applications.

Prof. Huang has been supported by The National Program for Support of Top-notch Young Professionals (2017), the China National Science Fund for Excellent Young Scholars (2015), and the New Century Excellent Talents in University from the Ministry of Education of China (2011). He was the recipient of the Boeing Award for the Best Paper in Image Analysis and Interpretation from the American Society for Photogrammetry and Remote Sensing (ASPRS) in 2010, the second place recipient for the John I. Davidson President's Award from ASPRS in 2018, and the National Excellent Doctoral Dissertation Award of China in 2012. In 2011, he was recognized by the IEEE Geoscience and Remote Sensing Society (GRSS) as the Best Reviewer of the IEEE GEOSCIENCE AND REMOTE SENSING LETTERS. He was the winner of the IEEE GRSS 2014 Data Fusion Contest. He was the Lead Guest Editor of the special issue on information extraction from high-spatial-resolution optical remotely sensed imagery for the IEEE JOURNAL OF SELECTED TOPICS IN APPLIED EARTH OBSERVATIONS AND REMOTE SENSING (vol. 8, no. 5, May 2015). Since 2014, he serves as an Associate Editor of the IEEE GEOSCIENCE AND REMOTE SENSING LETTERS.